water

Article

Three-Dimensional Numerical Simulation of Flow Structure in Annular Flume Based on CFD Study of Water

Jun Yan [1], Litao Zhang [1], Linjuan Xu [2,*], Sainan Chen [1], Guanghong Peng [3] and Meng Wang [1]

[1] School of Water Conservancy, North China University of Water Resources and Electric Power, Zhengzhou 450046, China
[2] Key Laboratory of Lower Yellow River Channel and Estuary Regulation, MWR, Yellow River Institute of Hydraulic Research, YRCC, Zhengzhou 450003, China
[3] Department of Power Grid Construction, Wuhan Electric Power Technical College, Wuhan 430072, China
* Correspondence: xlj2112003@163.com

Abstract: The annular flume is an ideal hydrodynamic test device for studying river sediment, and it has been widely used in recent years to study the movement patterns of sediment and other particulate matter. Annular flumes have made outstanding contributions to research in fields related to sediment transport and the diffusion and migration of pollutants. The existence of circumfluence structures in annular flumes leads to complex and variable flow structures. To obtain a more stable and controllable water flow structure, a sophisticated three-dimensional mathematical model based on the Fluent software was established to study the development law of water flow structure in the flume by changing the size of the annular flume speed ratio. The results show the following: (1) The overall trend of the simulation results basically matched with the measured results; the average relative error was 3.54% and the Nash efficiency coefficient was 0.9934, close to 1. The model calculation data were highly credible. (2) The axial flow velocity of the water tank gradually showed a "U"-shape distribution with the increase in the speed ratio. (3) When the speed ratio was $R \leq 0.17$ (where the speed ratio R refers to the ratio of annular groove to shear ring speed), there was only one vortex in the tank; when the speed ratio was $R > 0.17$, there were multiple vortices in the tank, and the flow pattern was more complicated. (4) When the rotational speed ratio $R = 0.28$, the secondary flow intensity of the annular flume reached the lowest point, which was only 39.28% of the secondary flow intensity of the conventional annular flume. (5) It was determined that the annular flume water flow structure was most stable and controllable when the rotational speed ratio $R = 0.24$. The results of the study can provide a further theoretical basis for research on sediment dynamics and its related fields conducted by applying an annular flume.

Keywords: annular flume; secondary flow; eddy flow; fluid–solid coupling; rotational speed ratio; water flow structure; VOF method

check for updates

Citation: Yan, J.; Zhang, L.; Xu, L.; Chen, S.; Peng, G.; Wang, M. Three-Dimensional Numerical Simulation of Flow Structure in Annular Flume Based on CFD Study of Water. *Water* **2023**, *15*, 651. https://doi.org/10.3390/w15040651

Academic Editor: Giuseppe Francesco Cesare Lama

Received: 9 December 2022
Revised: 6 February 2023
Accepted: 6 February 2023
Published: 7 February 2023

1. Introduction

The study of water flow structure is one of the fundamental areas in the study of particle movement laws, and a stable and controllable water flow structure provides ideal research conditions for sediment transport, pollutant migration, diffusion and other related fields. The annular flume has been widely used in recent years to study the movement patterns of sediment and other particles because it can meet the requirements of distance required for sedimentation and has no inflow port and flow outlet [1–4]. The traditional annular sink drive method is a one-way shear ring drive which will produce strong secondary flow due to the existence of the circumfluence structure, resulting in the uneven distribution of centrifugal force and pressure gradient [5,6]. The uneven distribution of centrifugal force and pressure gradient will affect the water flow structure of the annular flume, resulting in a large amount of siltation of sediment and other particles on the inner side of the flume [7–9]; the uneven distribution of siltation in the flume is not conducive to the study of the movement pattern of particles. Achieving a stable and controllable water flow structure using an annular flume in the study of particle motion law has become a popular research topic for many scholars.

In order to obtain a stable and controllable water flow structure in annular flumes, the driving method of the annular flume has been improved by previous scholars. By adjusting the speed ratio R between the shear ring and the annular flume to make the tracer sand (model sand, etc.) move in the midline and thus weaken the secondary flow disturbance in the flume, this research method provides a theoretical guide to study sediment movement in rivers [10–13]. However, physical model tests are less relevant when describing the flow regime and spatial variation of water flow compared to mathematical models [14,15]. To further investigate the flow structure of the annular flume, it is extremely important to carry out numerical simulation studies. By building a mathematical model of the annular flume and simulating it, more complete experimental data can be obtained compared with the physical model. More complete experimental data can provide a theoretical basis for further investigation of the water flow structure of the annular flume.

Numerical simulation of the annular flume was initially performed as a two-dimensional mathematical model, i.e., the annular flume was considered to be composed of numerous rectangular sections, and the flow structure of the entire annular flume was obtained by simulating the flow structure of one of the rectangular sections [16–18]. However, the vortex structure is three-dimensional in nature, and the two-dimensional mathematical model does not accurately simulate the vortex structure in the slot. Therefore, in order to study the water flow structure in the annular flume more accurately, it is more reasonable to use a 3D numerical simulation to study the water flow characteristics of the annular flume. The three-dimensional mathematical model of the annular flume has been studied extensively in recent years; for example, Su-Hyun Yang [19] used a three-dimensional mathematical model to determine the distribution of radial shear stresses at the bottom of the annular flume, and the results showed that in the reverse rotation mode of the flume and the shear ring, the rotation ratio of the upper ring to the flume had a more dramatic effect on the location and configuration of the two secondary flow cells and the resulting fluctuations in the flow field and bottom shear stresses. Olya Skulovich [20] developed a spatially averaged mathematical model of cohesive sediment erosion based on physical model tests in an annular flume, which allows prediction of the concentration of suspended matter in the aqueous phase and fitting functions applied to shear stress, sediment particle size distribution, abundance of rainbow trout per cubic meter of water, and various sediment bed properties.

Although a large number of studies have been conducted on the 3D mathematical model of the annular flume, a detailed study of the flow structure of the annular flume itself with respect to the speed ratio has not been conducted. Unclear water flow structure patterns will greatly affect the accuracy of the experimental results of the application of the annular flume. In order to obtain a stable and controllable water flow structure in the annular flume, this study analyzes the water flow structure of the annular flume under different rotational speed ratios using Fluent software as a prototype of the annular flume at Hohai University and focuses on the development of axial flow velocity and vortices in the flume as the rotational speed ratio of the flume increases. This study can provide technical support for the analysis of water flow structure and the development process of eddy flow. In addition, it can be used to provide a theoretical basis for studies in sediment transport, pollutant (e.g., microplastic) migration and diffusion and other related fields.

2. Model Development

2.1. Annular Sink Description and Instrumentation

Mathematical modeling of the annular flume was performed with reference to the physical model of the annular flume at Hohai University [21]. The physical model test setup is as follows: the outer and inner walls of the water tank and the bottom tank are cemented together, collectively referred to as the annular tank; the annular tank specifications are:

outer diameter $R1$ = 280 cm and inner diameter $R2$ = 240 cm (the specifications of the mathematical model device are the same as those of the physical test device of Hohai University). The driving method of the flume is driven by the shear ring and the annular groove together; the annular groove obtains the rotational speed with the increase in motor frequency during the test, the shear ring inside the groove can be lifted and lowered by hand, the lower wall of the shear ring is close to the water surface during the test, the rotational speed with the increase in motor frequency is obtained using the annular groove of different size and opposite direction, and the test water depth y = 30 cm (fluid temperature is 25 °C). The dimensions of the flume are shown in Figure 1.

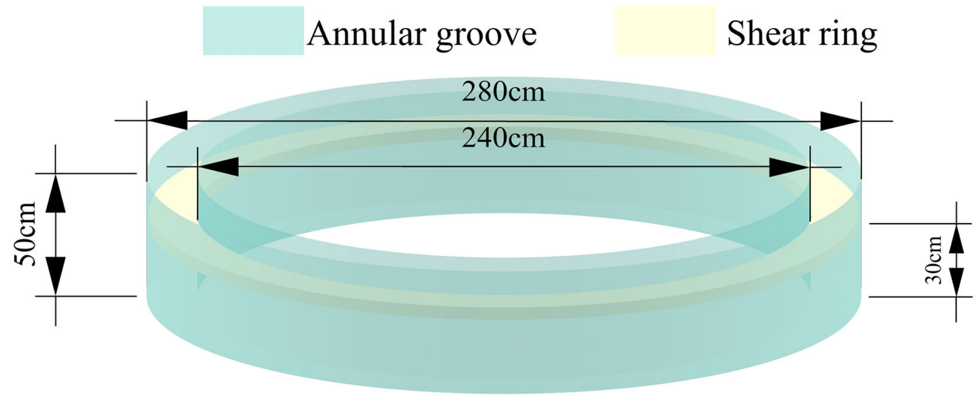

Figure 1. Dimensions of the ring sink model.

2.2. Model Selection and Governing Equations

The two equations for calculating turbulence in hydrodynamics are Large Eddy Simulation (LES) and Reynolds-averaged Navier–Stokes equations (RANS). Since RANS has the advantages of smaller computational effort and lower mesh quality requirement near the wall compared to LES, RANS was chosen as the equation for turbulence calculation in this study in order to save computational cost while ensuring the simulation quality [22,23].

The two commonly used turbulence models in hydrodynamics are the Renormalization Group k-ε Model (RNG k-ε model) and the Standard k-ε Model. The RNG k-ε model corrects the dissipation rate equation and performs better than the Standard k-ε Model for some complex shear flow, vortex, separation and other flow problems; therefore, the RNG k-ε turbulent model was used in this study [24,25]. The continuity equation, momentum equation and RNG k-ε equation for the turbulent flow model of the RNG k-ε equation can be expressed in the following equations:

Continuity equation:

$$\frac{\partial \rho}{\partial t} + \frac{\partial(\rho u_i)}{\partial x_i} = 0, \tag{1}$$

Conservation of momentum equation:

$$\frac{\partial(\rho u_1)}{\partial t} + div(\rho u_1 u_1) = div(\mu \text{ grad } u_1) - \frac{\partial \mathrm{p}}{\partial x_1} + S_{\mathrm{u}_1}, \tag{2}$$

$$\frac{\partial(\rho u_2)}{\partial t} + div(\rho u_2 u_2) = div(\mu \text{ grad } u_2) - \frac{\partial \mathrm{p}}{\partial x_2} + S_{\mathrm{u}_2}, \tag{3}$$

$$\frac{\partial(\rho u_3)}{\partial t} + div(\rho u_3 u_1) = div(\mu \text{ grad } \mathrm{u}_3) - \frac{\partial \mathrm{p}}{\partial x_3} + S_{\mathrm{u}_3}, \tag{4}$$

RNG k-ε model:

$$\frac{\delta(\rho K)}{\delta t} + \frac{\delta(\rho \overline{u}_j K)}{\delta x_j} = \frac{\delta}{\delta x_j}[(\mu + \frac{\mu_t}{\mathrm{Pr}_\varepsilon})\frac{\delta \varepsilon}{\delta x_j}] + P_K + G_K - \rho_\varepsilon - Y_M, \tag{5}$$

$$\frac{\delta(\rho\varepsilon)}{\delta t}+\frac{\delta(\rho\overline{u}_j\varepsilon)}{\delta x_i}=\frac{\delta}{\delta x_j}[\alpha_\varepsilon(\mu+\frac{\mu_t}{\mathrm{Pr}_\varepsilon})\frac{\delta\varepsilon}{\delta x_j}]+C_{\varepsilon1}\frac{\varepsilon}{K}(P_K+C_{\varepsilon3}G_b)-C^*{}_{\varepsilon2}\rho\frac{\varepsilon^2}{K}, \tag{6}$$

Turbulent viscosity model:

$$\mu_t=\rho C_\mu\frac{K^2}{\varepsilon}, \tag{7}$$

of which:

$$C^*{}_{\varepsilon2}=C_{\varepsilon2}+\frac{C_\mu\rho\eta^3(1-\frac{\eta}{\eta_0})}{1+\beta\eta^3},\ \eta=\frac{K}{\varepsilon}\overline{S},\ \overline{S}=\sqrt{2\overline{S_{ij}S_{ij}}},\ \overline{S_{ij}}=\frac{1}{2}(\frac{\delta\overline{u_i}}{\delta x_j}+\frac{\delta\overline{u_j}}{\delta x_j}).$$

In the equation: x_i, x_j denote the coordinate positions when i or j is 1, 2, and 3, respectively, denoting the three x, y, and z directions; u_i denotes the velocity in the x_i direction; ρ is the density; t is the time; p is the pressure on the fluid micro-element; μ denotes the viscosity coefficient; S_{u_i} is denoted as the generalized source term of the momentum conservation equation; G_k denotes the turbulent kinetic energy due to the laminar velocity gradient; G_b denotes the turbulent kinetic energy due to buoyancy; and Y_m denotes the fluctuations generated by the diffusion of the transition in compressible turbulence. The model constants $C_{1\varepsilon}$, $C_{2\varepsilon}$, C_μ, α_K, α_ε, $C_{\varepsilon1}$, $C_{\varepsilon2}$, η_0 and β for the above equations take the values 1.44, 1.92, 0.0845, 1.39, 1.39, 1.42, 1.68, 4.377 and 0.012, respectively.

2.3. Calculation Methods and Boundary Conditions

In this study, Fluent was used to simulate the water–gas two-phase flow in the annular flume, which is driven by the annular flume and the shear ring in both directions. The boundary conditions were wall conditions, and the side walls were non-slip walls, where the annular flume and the shear ring were set to rotate around the reference system in the form of moving walls. The grid below the shear ring was selected as an adaptive grid to divide the water-filled region, and the water volume was filled by local initialization. To obtain the free fluid surface, the most commonly used method is the volume of fluid (VOF) method [26–28], but the VOF method is time-consuming to calculate; thus, to simplify the calculation, the rigid-lid approximation was implemented, which is effective for subcritical flow with Fr < 0.36 [29]. The model calculation method was set to transient calculation, the momentum equation was solved by upward discretization, the pressure-velocity coupling was solved by the PISO algorithm, the time step was set to 0.001 s and residual values were less than 1×10^{-4}. (All of the above were set up in the ANSYS Fluent software; details can be found in Ansys Resource Center | Webinars, White Papers and Articles.)

2.4. Mesh Profiling

The annular flume calculation mesh was generated by the software ICEM CFD, and the mesh type was a hexahedral structural mesh. When considering the RNG k-ε turbulent flow mathematical model for near-wall fluid calculations using the wall function method, a disadvantage is its lack of accuracy of fluid calculations near the wall. In order to improve the accuracy of fluid calculation near the wall, the mesh near the wall is locally encrypted and the number of cells can reach 202,452; after generating the mesh, a refinement procedure increases the mesh quality to above 0.8. The annular flume grid profile is shown in Figure 2.

2.5. Grid Convergence Analysis

The simulated average flow velocity ($\overline{vr}$) calculated from nine points monitored in the physical model test of the annular flume at the University of Shanghai was used as a control, and a working condition with a water level of 30 cm and a midline flow velocity of 58.8 cm/s at the bottom was selected. By adjusting the model grid size and comparing the error between the numerical simulation mean flow velocity $\overline{u}$ and the measured mean flow velocity $\overline{u_R}$, a grid-independence analysis was performed to find the optimal solution for the model grid size. The specific grid size selection data are shown in Table 1.

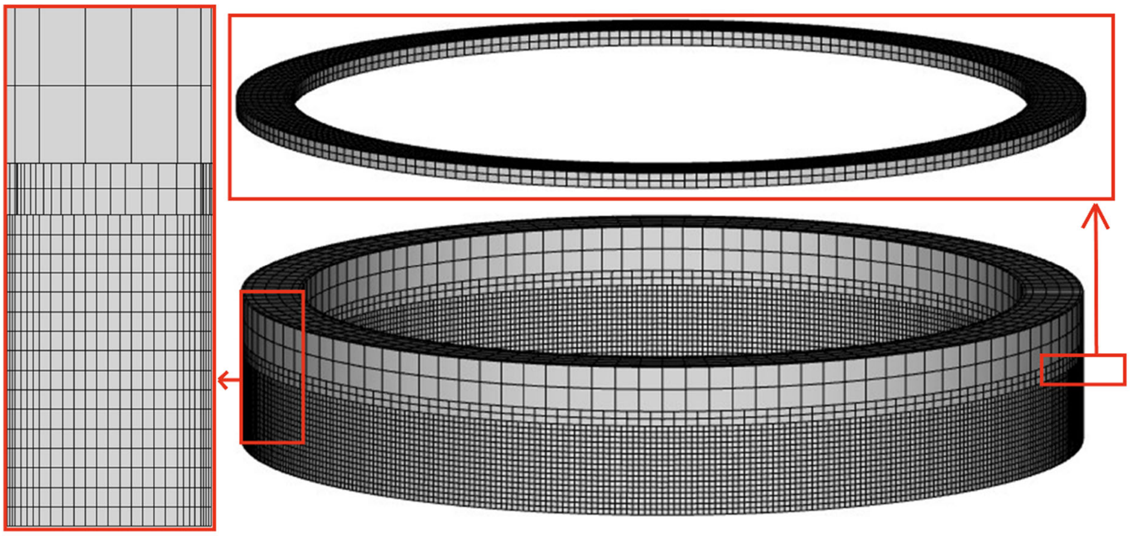

Figure 2. Calculation area of the mesh profile.

Table 1. Grid irrelevance verification table.

Scheme	Grid Size/cm	Local Encryption	$\overline{u}$/cm·s^{-1}	$\overline{u_R}$/cm·s^{-1}	Error
A	3	No	130.21	94.04	38.47%
B	1	No	103.92	94.04	10.51%
C	1	Yes	97.37	94.04	3.54%
D	0.5	No	97.31	94.04	3.48%

As can be seen from Table 1, the error of scheme A was as large as 38.47%. Tofurther improve the calculation accuracy, the overall grid size was encrypted to 1 cm again to obtain scheme B, which reduced the error to 10.51%. Scheme C considers that the RNG k-ε turbulent model has poor calculation accuracy for the grid near the wall so the grid size near the wall was locally encrypted to 0.5 cm, which further decreased the error to 3.54%. The overall grid size of scheme D was 0.5 cm, and the error was reduced to 3.48% without local encryption, an improvement of only 0.06% compared with scheme C, but increased the difficulty of numerical model calculation. The simulation time increased from one and a half days to three and a half days for the simulation time cost of a single working condition, which greatly increased the time cost. Therefore, scheme C was adopted for the annular flume mesh dissection scheme.

2.6. Model Validation

Before the simulation analysis, in order to ensure realistic and reliable simulation results, model validation was carried out with the relevant physical model results. Since the RNG k-ε turbulent flow mathematical model was not accurate enough to calculate the fluid near the wall, and there was a large flow velocity gradient near the wall, the midline flow velocity in the flume was selected as the measured value. The model was validated using two parameters: the Nash–Sutcliffe efficiency coefficient and the relative error [30–32]. The comparison of the measured and simulated results is shown in Figure 3, where y denotes the height.

Comparing the numerical simulation results with the physical model test results, the curves were found to be in basic agreement with the scatter, with an average relative error of 3.54%. It is worth noting that the measured values in the range of $0.25 < y < 0.275$ m showed large errors with the simulated values, but the maximum relative error did not exceed 16%. The reason for this result is that the flow velocity meter used in the literature is a rotating paddle-type flow velocity meter; the rotating paddle flow meter has a disturbing effect on the water flow [33–35] and this point is close to the shear ring, where the surrounding fluid has a large flow velocity gradient, resulting in a large difference between the measured and simulated results at this point. However, the overall trend of the simulation results basically matched with the measured results, and the calculated Nash efficiency coefficient was 0.9934, which is close to 1. This proves that the model is credible and can be used for subsequent studies.

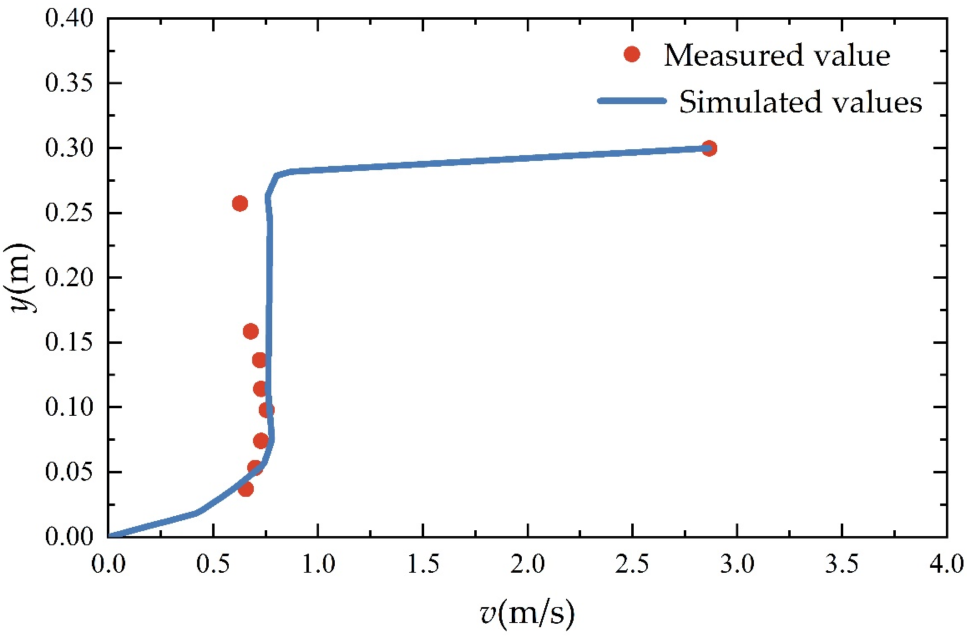

Figure 3. Comparison of simulation and test results.

3. Simulation Results and Analysis

3.1. Cross-Sectional Axial Flow Velocity Contour Distribution

The cross-sections analyzed in Figure 4 were obtained by slicing with Tecplot post-processing software. The left side of the cross section is the outer wall side, and the right side is the inner wall side. Figure 4a shows the control group with the shear ring speed of 0.35 rad/s and the annular groove kept stationary; Figure 4b–l shows the working conditions with different speed ratios obtained by gradually increasing the annular groove speed while keeping the shear ring speed constant. As can be seen in Figure 4, as the speed ratio increases, the region of reverse flow velocity gradually surrounds the region of forward flow velocity (the axial flow velocity in the same direction as the shear ring rotation is the forward flow velocity, and the reverse flow velocity is vice versa), the axial flow velocity contour map from the zero value of axial flow velocity as the boundary gradually shows a "U"-type distribution, where the opposite direction of the shear ring rotation speed of the water from the side wall to the center of the tank expansion is seen, and the expansion speed of the inner wall side is greater than the outer wall side.

3.2. Cross-Sectional Velocity Vector Distribution

The cross-sectional velocity vector distribution was obtained by uniformly extracting the flow velocity data at 10,000 points at each speed ratio, and then integrating and analyzing the data to obtain the velocity vector distribution and the trend of the Reynolds number at different speed ratios. As can be seen from Figure 5, when the speed ratio $R \leq 0.17$, there is only one vortex in the section, and when the speed ratio $R > 0.17$, multiple vortices start to appear, and the flow pattern becomes more complex. The transition from stable to complex water flow patterns must be accompanied by an increase in the Reynolds number. As can be seen from Figure 6, if the Earth is used as the reference system, the axial velocity is absolute, and the Reynolds number decreases with the increase in the speed ratio at this time, which is not in line with the objective law presented in the cross-sectional vector diagram in Figure 5. If the reverse flow velocity maximum value is used as the standard value, and the absolute value of each point and the standard value are subtracted so as to obtain the relative value of the axial flow velocity, the Reynolds number increases with the increase in the speed ratio in line with the objective law presented in the vector diagram in Figure 5. The reason for this difference is that the annular groove rotates at a certain angular velocity while giving a certain reverse flow rate to the water near the wall of the annular groove. The relative value of axial flow velocity is more in line with the natural law than with the absolute value of axial flow velocity.

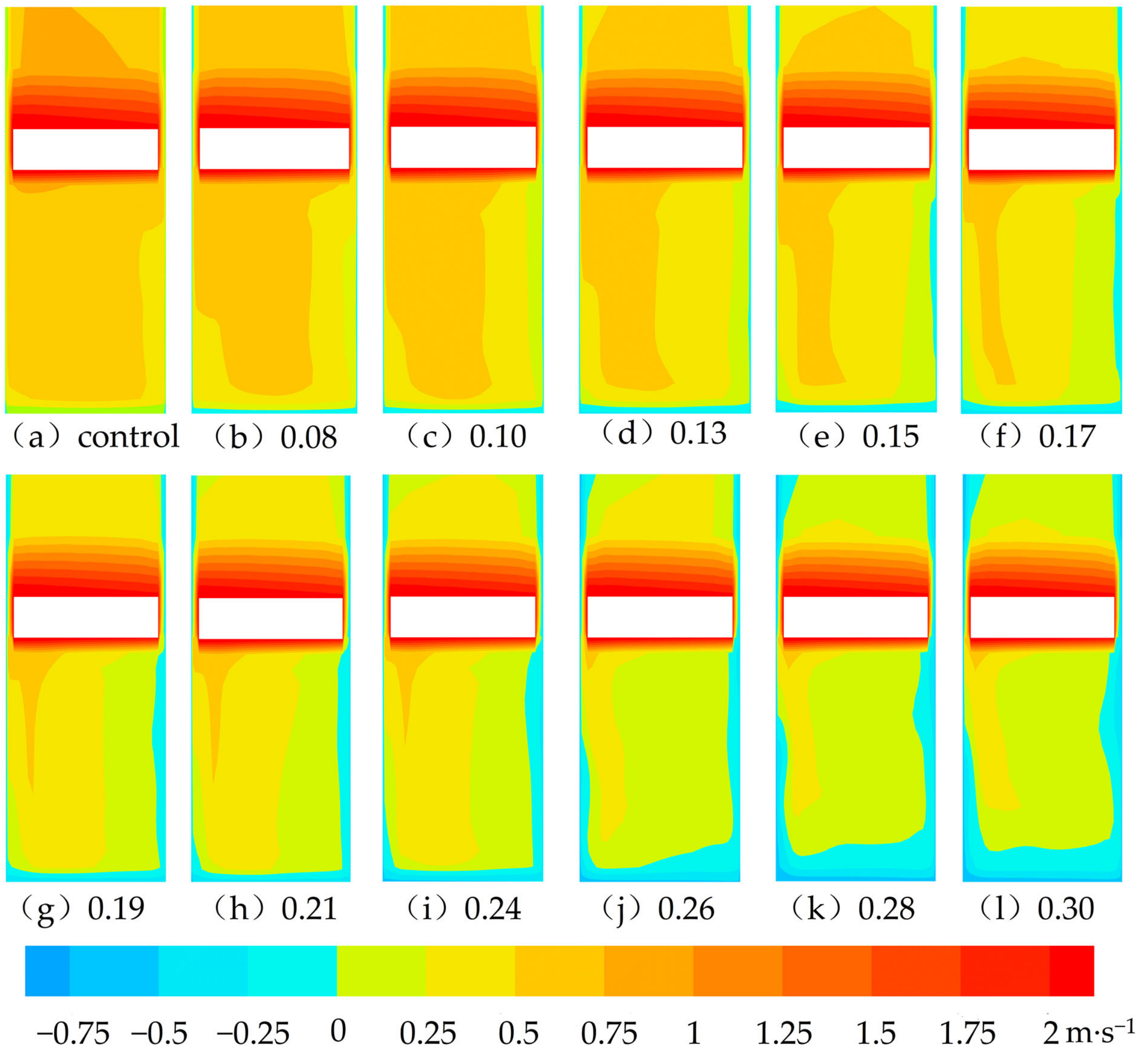

Figure 4. Contour distribution of axial flow velocity in annular flume at different speed ratios, where (**a**) is the control group driven by the shear ring only; (**b**–**l**) are the different working conditions obtained by different turn–continuity ratios.

3.3. Shear Force Distribution at the Bottom of the Flume

In order to examine the effect of the change of water flow structure on the distribution of truncated shear forces at the bottom of the flume, six sets of bottom shear force distribution curves with different speed ratios were plotted in this study using the turbulent kinetic energy method. As can be seen from Figure 7, when the rotational speed ratio $R < 0.15$, the bottom shear distribution is more regular, and the peak of the bottom shear occurs near the midline ($-1.32 < x < -1.30$ m). When the speed ratio is $0.15 < R < 0.24$, the bottom shear force on the near inner wall side grows significantly faster than that on the inner wall side, and the bottom shear force gradually shows a more obvious bimodal distribution (the peak near the midline is the main peak, and the peak on the near wall side is the secondary peak).

When the rotational speed ratio $R = 0.24$, the sub-peak peak value gradually approaches that of the main peak, and the shear force distribution at the bottom of the flume tends to be flat. Compared with the working condition of $R = 0.28$ and $R = 0.24$, the shear force at the bottom of the near outer wall side shows a significant decay, and the shear force at the bottom of the flume shows a single-peak distribution, with the peak occurring at the near inner wall measurement, and the shear force at the bottom of the flume is extremely unevenly distributed.

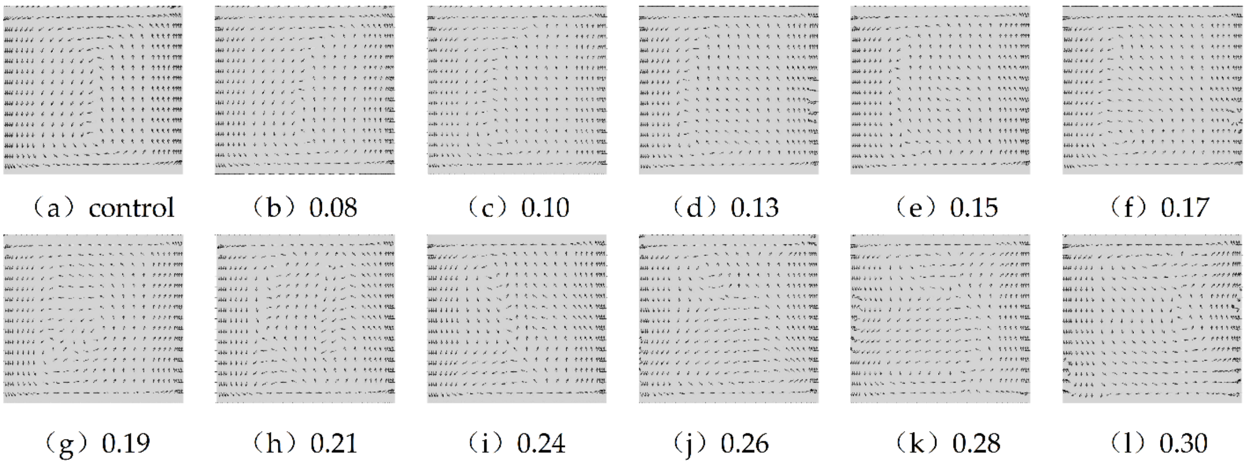

Figure 5. Velocity vector distribution in the flume at different speed ratios.

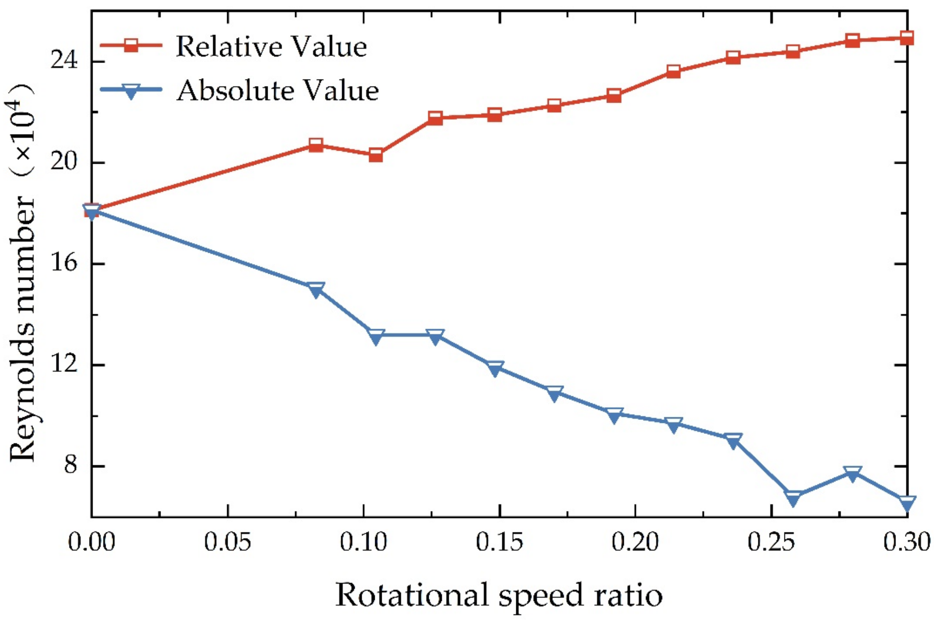

Figure 6. Trend of Reynolds number of water flow in the flume at different speed ratios.

In summary, the different speed ratios of the annular flume greatly affect the bottom shear force distribution pattern. A speed ratio of $R \leq 0.24$ is when the speed ratio and the size of the bottom shear show a positive correlation, and the bottom shear distribution tends to be flat; the speed ratio $R = 0.24$ when the bottom shear distribution is the most uniform; the speed ratio is $R > 0.24$ when the bottom shear distribution abruptly changes, such that the size of the bottom shear measured near the inner wall further increases near the outer wall side of the bottom shear but decays, and the bottom shear distribution of the flume is extremely uneven. When the velocity ratio $R = 0.24$, the bottom shear force is most uniformly distributed. Additionally, the secondary flow intensity under this condition is 47.24% of the secondary flow intensity of the annular flume driven by the shear ring, which is not much different from the secondary flow intensity of the annular flume with the velocity ratio $R = 0.28$. It can be determined that the annular flume water flow structure is most stable and controllable when the velocity ratio is $R = 0.24$.

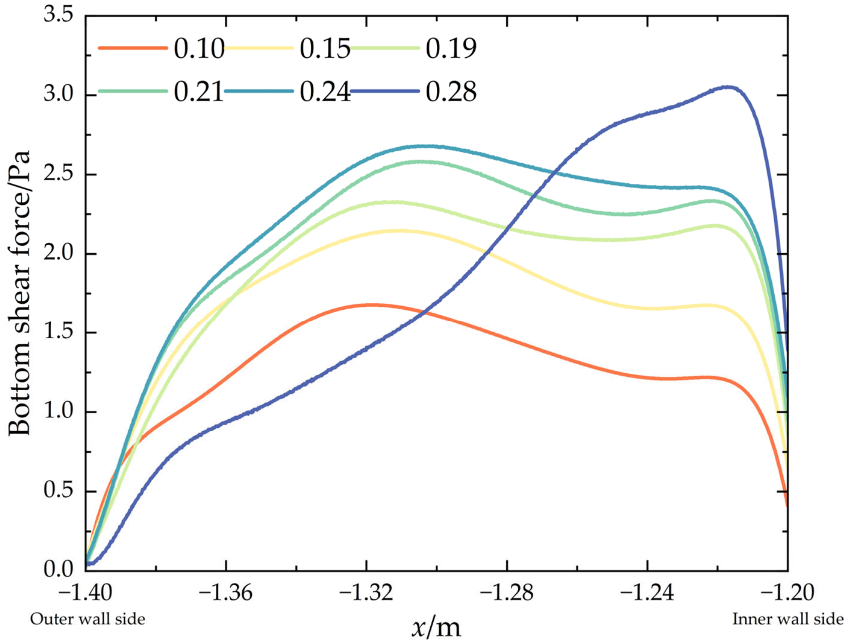

Figure 7. Distribution of shear force at the bottom of the flume at different speed ratios, where x is the distance from the center of the circle.

3.4. The Variation Pattern of Secondary Flow Intensity with the Size of Speed Ratio

Secondary flow refers to a flow that produces a deflection parallel to the boundary, superimposed on the axial flow velocity. The ratio of deflected flow velocity to axial flow velocity is commonly used in academia to discern the magnitude of secondary flow. Figure 8 shows the distribution of deflected flow velocity in the longitudinal section, and it can be observed that the larger deflected flow velocity ($|$deflected flow velocity$|$ > 0.02 m/s^2) is concentrated near the bottom of the flume and the water surface ($0 < y < 0.05$ m vs. $0.025 < y < 0.3$ m), as shown in Figure 9. The intensity of secondary flow at the bottom of the sink and the surface water both decrease with the increase in the speed ratio, and the intensity of secondary flow at the bottom of the sink is greater than that of the surface water, with the increase in the speed ratio R and the weakening trend of secondary flow at the bottom of the sink being more obvious than that near the water surface, so $0 < y < 0.05$ m of the bottom of the sink was chosen as the key study area of secondary flow intensity.

Combined with Figures 5 and 9, the following can be observed: (1) When only the shear ring was driven, the water flow in the flume produced a sub-flow with the surface layer outward and the bottom layer inward, and the sediment at the bottom of the flume mainly silted up on the inner wall side. (2) When the rotational speed ratio $R < 0.28$, the state of vortex motion at the bottom of the annular flume was counterclockwise rotation; with the increase in the rotational speed ratio, the trend of water flow at the bottom of the annular flume towards the inner wall gradually decreased. (3) When the rotational speed ratio $R = 0.28$, the trend of water flow at the bottom of the inner wall side showing movement toward the inner wall weakened along the course, and two vortices in opposite directions were formed at the bottom of the flume, which canceled each other at a distance of 13 cm from the outer wall, at which time the sediment moved to the center of the flume, greatly offsetting the effect of the secondary flow. (4) The minimum secondary flow intensity in the flume at the speed ratio $R = 0.28$ was only 39.28% of the secondary flow intensity in the shear ring-driven annular flume. (5) At the speed ratio $R = 0.28$, the minimum secondary flow intensity in the flume was only 47.24% of the secondary flow intensity in the shear ring-driven annular flume. (6) When the speed ratio reached $R \geq 0.3$, the bottom vortex began to rotate mainly clockwise, and the intensity of the secondary flow began to increase.

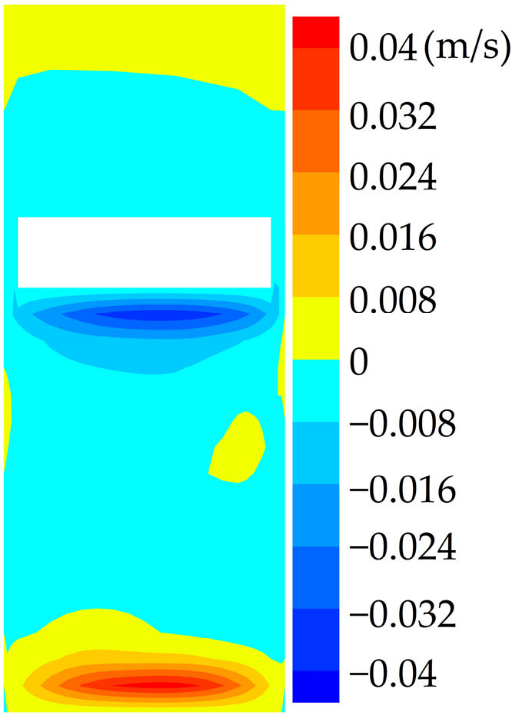

Figure 8. Contour variation of deflected flow velocity.

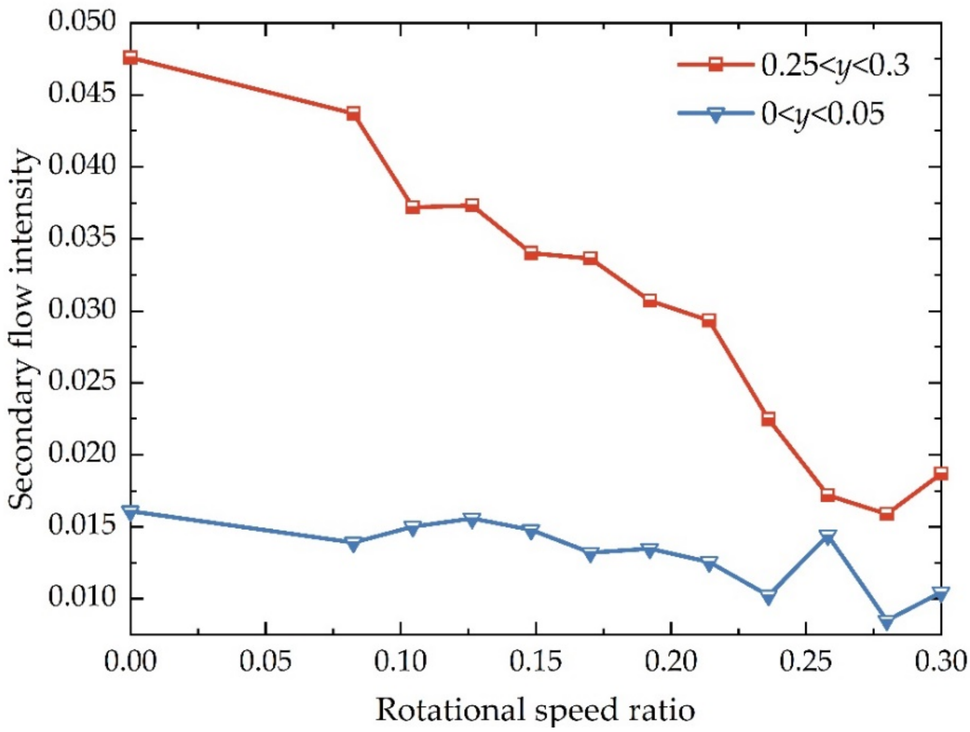

Figure 9. Secondary flow intensity at different speed ratios.

4. Conclusions

Based on the three-dimensional numerical model, the following conclusions can be obtained by studying and analyzing the water flow structure of the annular flume under different working conditions:

(1) As the speed ratio increases, the negative flow velocity gradually expands from the side wall to the center of the flume, the axial flow velocity of the annular flume gradually shows a "U"-type distribution and the axial flow velocity distribution becomes more uniform. The relative value of axial flow velocity is more in line with the natural law than the absolute value of axial flow velocity for the calculation of the Reynolds number. In addition, in terms of water flow structure stability, the water flow structure is more complex as the speed ratio increases.

(2) When the speed ratio $R \leq 0.24$, the speed ratio and the bottom shear size show a positive correlation, and the bottom shear distribution tends to be flat. The speed ratio $R = 0.24$ is the critical point when the bottom shear distribution is most uniform; when $R > 0.24$, the bottom shear peak position is shifted to the inner wall side, the bottom shear distribution is extremely uneven, and the sediment is more likely to accumulate on the outer wall side at this time.

(3) When the speed ratio $R < 0.28$, the secondary flow intensity shows a negative correlation with the size of the speed ratio. When the speed ratio $R = 0.28$, the secondary flow intensity of the annular sink reaches the lowest value, which is only 39.28% of the secondary flow intensity of the annular sink driven by the shear ring. When the velocity ratio $R = 0.24$, the annular flume water flow structure is the most stable and controllable.

(4) Compared with the previous research results, this study investigates the axial flow velocity and the development of vortex flow in the flume with increasing speed ratios in more detail. This study can provide technical support for research in sedimentation, pollutant release, transport and dispersion and other related scientific fields.

Author Contributions: Conceptualization, J.Y. and L.Z.; methodology, L.Z.; software, M.W. and L.X.; validation, J.Y.; formal analysis, S.C.; investigation, L.Z.; resources, M.W.; data curation, L.Z.; writing—original draft preparation, L.Z.; writing—review and editing, G.P.; visualization, M.W.; supervision, L.Z.; project administration, J.Y.; funding acquisition, J.Y.; writing—review and editing, L.Z. All authors have read and agreed to the published version of the manuscript.

Funding: This research was supported by the Special Project of National Natural Science Foundation of China (42041006), the National Natural Science Foundation of China (U2243220), the Excellent Youth Foundation of He' nan Scientific Committee (222300420013), the Excellent Young Talents Project of Yellow River Conservancy Commission (HQK-202309) and the Special Basic Research Fund for Central Public Research Institutes (HKY-JBYW-2020-15).

Data Availability Statement: The data presented in this study are available on request from the corresponding authors.

Acknowledgments: We would like to thank the potential reviewer very much for their valuable comments and suggestions. We thank my other colleagues' valuable comments and suggestions that have helped improve the manuscript. We also thank Yellow River Institute of Hydraulic Research for financial support.

Conflicts of Interest: The authors declare no conflict of interest.

References

1. Bale, A.J.; Widdows, J.; Harris, C.B.; Stephens, J.A. Measurements of the critical erosion threshold of surface sediments along the Tamar Estuary using a mini-annular flume. *Cont. Shelf Res.* **2006**, *26*, 1206–1216. [CrossRef]
2. Droppo, I.G.; di Cenzo, P.; Parrott, J.; Power, J. The Alberta oil sands eroded bitumen/sediment transitional journey: Influence on sediment transport dynamics, PAH signatures and toxicological effect. *Sci. Total Environ.* **2019**, *677*, 718–731. [CrossRef] [PubMed]
3. Xu, C.; Chen, Y.; Pan, Y.; Yu, L. The effects of flocculation on the entrainment of fluid mud layer. *Estuar. Coast. Shelf Sci.* **2020**, *240*, 106784. [CrossRef]

4. Hu, Y.; Chen, J.; Wang, C.; Wang, P.; Gao, H.; Zhang, J.; Zhang, B.; Cui, G.; Zhao, D. Insight into microbial degradation of hexabromocyclododecane (HBCD) in lake sediments under different hydrodynamic conditions. *Sci. Total Environ.* **2022**, *827*, 154358. [CrossRef] [PubMed]
5. Abduo, S.S.; Elmoustafa, A.M.; Salam, M.S.A. Study of counteracting the secondary flow in open channel bends. *Ain Shams Eng. J.* **2021**, *12*, 2425–2433. [CrossRef]
6. Yang, Z.; Baptista, A.; Darland, J. Numerical modeling of flow characteristics in a rotating annular flume. *Dyn. Atmos. Ocean.* **2000**, *31*, 271–294. [CrossRef]
7. Zhao, Y.; Wang, Y.; Yao, J. Effect of turbulence-driven secondary flow on particle preferential concentration and clustering in turbulent square duct flows. *Particuology* **2021**, *55*, 70–83. [CrossRef]
8. Yin, H.-L.; Qiu, M.-Y.; Xu, Z.-X. Study on transport of powdered activated carbon using a rotating circular flume. *J. Hydrodyn. Ser. B* **2013**, *25*, 772–777. [CrossRef]
9. Guo, C.; Manning, A.J.; Bass, S.; Guo, L.; He, Q. A quantitative lab examination of floc fractal property considering influences of turbulence, salinity and sediment concentration. *J. Hydrol.* **2021**, *601*, 126574. [CrossRef]
10. Huang, J.; Ge, X.; Wang, D. Distribution of heavy metals in the water column, suspended particulate matters and the sediment under hydrodynamic conditions using an annular flume. *J. Environ. Sci.* **2012**, *24*, 2051–2059. [CrossRef]
11. Pope, N.D.; Widdows, J.; Brinsley, M.D. Estimation of bed shear stress using the turbulent kinetic energy approach—A comparison of annular flume and field data. *Cont. Shelf Res.* **2006**, *26*, 959–970. [CrossRef]
12. Wang, H.; Zhao, Y.; Wang, X.; Liang, D. Fluctuations in Cd release from surface-deposited sediment in a river-connected lake following dredging. *J. Geochem. Explor.* **2017**, *172*, 184–194. [CrossRef]
13. Ramalingam, S.; Chandra, V. Influence of live microbes on suspended sediment concentration in coastal ecosystem. *Mar. Geol.* **2018**, *405*, 108–113. [CrossRef]
14. Wang, Q.; Li, M.; Xu, W.; Yao, L.; Liu, X.; Su, D.; Wang, P. Review on liquid film flow and heat transfer characteristics outside horizontal tube falling film evaporator: Cfd numerical simulation. *Int. J. Heat Mass Transf.* **2020**, *163*, 120440. [CrossRef]
15. Bordbar, A.; Taassob, A.; Zarnaghsh, A.; Kamali, R. Slug flow in microchannels: Numerical simulation and applications. *J. Ind. Eng. Chem.* **2018**, *62*, 26–39. [CrossRef]
16. James, P.W.; Jones, T.E.R.; Stewart, D.M. Numerical and experimental studies of annular flume flow. *Appl. Math. Model.* **1996**, *20*, 225–231. [CrossRef]
17. Booij, R. Large eddy simulation of flows in some curved flumes. In *Engineering Turbulence Modelling and Experiments 5*; Rodi, W., Fueyo, N., Eds.; Elsevier Science Ltd: Oxford, UK, 2002; pp. 347–356.
18. Maa, J.P.Y. Discussion on the article "Numerical modeling of flow characteristics in a rotating annular flume" by Yang, Z., Baptista, A., Darland, J. [Dyn. Atmos. Oceans 31 (2000) 271–294]. *Dyn. Atmos. Ocean.* **2001**, *33*, 321–323. [CrossRef]
19. Yang, S.-H.; Im, I.-T.; Hwang, K.-N.; Cho, Y.-S.; Ryu, H.-R. A numerical study on optimal rotation ratio and bottom shear stress in the counter-rotation mode of an annular flume. *J. Hydro-Environ. Res.* **2015**, *9*, 473–481. [CrossRef]
20. Skulovich, O.; Cofalla, C.; Ganal, C.; Schüttrumpf, H.; Ostfeld, A. Modelling of resuspension due to fish activity: Mathematical modeling and annular flume experiments. *Int. J. Sediment Res.* **2017**, *32*, 421–431. [CrossRef]
21. Wang, J.; Zhou, J.; Zhang, C.J.J.o.S.R. Experimental study on velocity distribution of two-direction rotating annular flume. *J. Sediment Res.* **2014**, *5*, 32–37. [CrossRef]
22. Goodarzi, D.; Abolfathi, S.; Borzooei, S. Modelling solute transport in water disinfection systems: Effects of temperature gradient on the hydraulic and disinfection efficiency of serpentine chlorine contact tanks. *J. Water Process Eng.* **2020**, *37*, 101411. [CrossRef]
23. Goodarzi, D.; Mohammadian, A.; Pearson, J.; Abolfathi, S. Numerical modelling of hydraulic efficiency and pollution transport in waste stabilization ponds. *Ecol. Eng.* **2022**, *182*, 106702. [CrossRef]
24. Analytis, G.T. Implementation and assessment of the renormalization group (RNG), quadratic and cubic non-linear eddy viscosity k–ε models in GOTHIC. *Nucl. Eng. Des.* **2001**, *210*, 177–191. [CrossRef]
25. Dyck, N.J.; Parker, M.J.; Straatman, A.G. The impact of boundary treatment and turbulence model on CFD simulations of the Ranque-Hilsch vortex tube. *Int. J. Refrig.* **2022**, *141*, 158–172. [CrossRef]
26. Xiao, H.; Huang, W.; Tao, J.; Liu, C. Numerical modeling of wave–current forces acting on horizontal cylinder of marine structures by VOF method. *Ocean. Eng.* **2013**, *67*, 58–67. [CrossRef]
27. Garoosi, F.; Mahdi, T.-F. Numerical simulation of three-fluid Rayleigh-Taylor instability using an enhanced Volume-Of-Fluid (VOF) model: New benchmark solutions. *Comput. Fluids* **2022**, *245*, 105591. [CrossRef]
28. Garoosi, F.; Mahdi, T.-F. New benchmark problems for validation and verification of incompressible multi-fluid flows based on the improved Volume-Of-Fluid (VOF) method. *Colloids Surf. A Physicochem. Eng. Asp.* **2022**, *648*, 129313. [CrossRef]
29. Oliveira, L.E.D.; da Costa, F.R.; Gualtieri, C.; Janzen, J.G. Effects of Vegetation Density on Sediment Transport in Lateral Cavities. *Environ. Sci. Proc.* **2022**, *21*, 16. [CrossRef]
30. Banihabib, M.E.; Vaziri, B.; Javadi, S. A model for the assessment of the effect of mulching on aquifer recharging by rainfalls in an arid region. *J. Hydrol.* **2018**, *567*, 102–113. [CrossRef]
31. Filippucci, P.; Brocca, L.; Bonafoni, S.; Saltalippi, C.; Wagner, W.; Tarpanelli, A. Sentinel-2 high-resolution data for river discharge monitoring. *Remote Sens. Environ.* **2022**, *281*, 113255. [CrossRef]
32. Pini, M.; Scalvini, A.; Liaqat, M.U.; Ranzi, R.; Serina, I.; Mehmood, T. Evaluation of Machine Learning Techniques for Inflow Prediction in Lake Como, Italy. *Procedia Comput. Sci.* **2020**, *176*, 918–927. [CrossRef]

33. Lam, W.H.; Robinson, D.J.; Hamill, G.A.; Johnston, H.T. An effective method for comparing the turbulence intensity from LDA measurements and CFD predictions within a ship propeller jet. *Ocean. Eng.* **2012**, *52*, 105–124. [CrossRef]
34. Chen, Y.; Wang, L.; Hua, H.X. Longitudinal vibration of marine propeller-shafting system induced by inflow turbulence. *J. Fluids Struct.* **2017**, *68*, 264–278. [CrossRef]
35. Liao, F.; Wang, S.; Yang, X.; He, G. A simulation-based actuator surface parameterization for large-eddy simulation of propeller wakes. *Ocean. Eng.* **2020**, *199*, 107023. [CrossRef]